International Journal of Solids and Structures 204–205 (2020) 52–64

Contents lists available at ScienceDirect

International Journal of Solids and Structures

journal homepage: www.elsevier.com/locate/ijsolstr

Micron-scale experimental-numerical characterization of metal-polymer interface delamination in stretchable electronics interconnects

S.M. Kleinendorst [a], R. Fleerakkers [a,1], E. Cattarinuzzi [b], P. Vena [b], D. Gastaldi [b], M.P.F.H.L. van Maris [a], J.P.M. Hoefnagels [a,*]

[a] Eindhoven University of Technology, Dept. of Mechanical Engineering, The Netherlands
[b] Politecnico di Milano, Dept. of Chemistry, Materials and Chemical Engineering, Italy

A R T I C L E I N F O

Article history:
Received 18 November 2019
Received in revised form 22 July 2020
Accepted 13 August 2020
Available online 19 August 2020

Keywords:
Interface delamination
Stretchable electronics
Cohesive zones
Experimental characterization
Numerical characterization
Mode mixity
Digital height correlation
Buckling

A B S T R A C T

Understanding the mechanical behavior and failure mechanisms of stretchable electronics is key in developing reliable and long-lasting devices. In this work a micron-scale stretchable system consisting of an aluminum serpentine patterned interconnect adhered to a polyimide substrate is studied. In-situ experiments are performed where the stretchable sample is elongated, while the surface topography is measured using a confocal microscope. From the resulting height profiles the microscopic three-dimensional deformations are extracted using an adaptive isogeometric digital height correlation algorithm. The displacement information is compared to realistic numerical simulations, in which the interface behavior is described by cohesive zone elements. It is concluded that despite fitting the traction separation law parameters, the model fails to correctly capture the distinct out-of-plane buckling (with magnitude of a few micron) of the interconnect. The model is updated with residual stresses resulting from processing and crystal plasticity induced behavior (decreased yield strength) in the aluminum layer, but both measures are not resulting in the experimentally observed deformations. Finally, mixed-mode cohesive zones are implemented, in which the properties are different in the shear and normal direction. After fitting the corresponding parameters to the experimental data, the model shows realistic in-plane and out-of-plane deformations. Also a predictive simulation for a different geometry results in the correct experimentally measured behavior. It is concluded that the aluminum-polyimide interface mode-angle dependency explains the observed microscopic failure mode of local delamination and buckle formation.
© 2020 The Authors. Published by Elsevier Ltd. This is an open access article under the CC BY license (http://creativecommons.org/licenses/by/4.0/).

1. Introduction

A relatively new and evolving direction for electronic applications is the development of highly deformable systems, i.e., stretchable electronics. Flexible and stretchable electronic devices are mainly used in biomedical applications, in order to bridge the gap between traditionally rigid, flat electronics and soft, curved biological tissue (such as skin and organs). Examples include patches that are adhered to human skin for health monitoring (Kim et al., 2011; Koh et al., 2016), flexible devices for cardiac diagnostics (Sterken et al., 2011; Gutbrod et al., 2014), smart contact lenses (Quintereo et al., 2017) and stretchable surgical tools, such as a balloon catheter with sensors for blood flow monitoring (Kim et al., 2011; Klinker et al., 2015). Other examples outside the biomedical field are smart textiles (Stoppa and Chiolerio, 2014), flexible displays (Rogers and Bao, 2002) and solar cells (Lipomi et al., 2012), multi-functional flexible patches (Yang et al., 2018) and LED arrays (Vanfleteren et al., 2012).

Often a stretchable electronics design consists of functional IC (integrated circuit) islands, e.g., sensors, actuators or microprocessors, that are connected by stretchable interconnects (electrical conductive wires), which encompass a thin metal film that is patterned in a meander shape on or encapsulated in a compliant, polymeric, substrate (Gonzalez et al., 2008; Gray et al., 2004). Elongation of these structures results in bending, twisting and stretching of the initially planar interconnect, inducing large deformations of the substrate, while only small strains are introduced in the metal film (Li et al., 2005). To ensure reliability and sufficient lifetime, it is important to investigate the mechanics of the stretchable devices (Harris et al., 2016). One of the main failure mechanisms is delamination between the interconnect and the substrate (Hsu et al., 2010), which is intrinsically coupled to

* Corresponding author at: Eindhoven University of Technology, Gemini-Zuid 4.122, 5600MB Eindhoven, The Netherlands.
E-mail address: j.p.m.hoefnagels@tue.nl (J.P.M. Hoefnagels).
[1] S.M. Kleinendorst and R. Fleerakkers are joined first authors.

https://doi.org/10.1016/j.ijsolstr.2020.08.011
0020-7683/© 2020 The Authors. Published by Elsevier Ltd.
This is an open access article under the CC BY license (http://creativecommons.org/licenses/by/4.0/).

buckling of the metal layer, followed by ductile failure of the interconnect, which in turn leads to complete failure of the electronic device (van der Sluis et al., 2018). Most experimental studies of stretchable electronics look at failure from a global perspective, i.e., at which global stretch percentage the interconnects fail, e.g., (Gray et al., 2004; Li et al., 2005; Hsu et al., 2010). However, to understand the failure mechanisms, micron-scale in situ testing is required, to study failure at the small scale of the damage. In literature multiple studies can be found towards experimental investigation of delamination in metal-polymeric interfaces, i.a., for copper-PDMS systems, where peel tests reveal fibrillation of the PDMS (Poly(dimethylsiloxane)), which induces remarkably high (macroscopically observed) interface toughness (Hoefnagels et al., 2010; van der Sluis et al., 2011; Neggers et al., 2015; Neggers et al., 2015). Also buckling-based failure of stretchable electronics has been investigated experimentally, where the influence of meander geometry on the failure modes is studied (Lucchini et al., 2016; Cattarinuzzi et al., 2015; Cattarinuzzi et al., 2015). Furthermore, numerical simulations have been performed to model the mechanical behavior of stretchable electronics. Some simulations are dedicated to a realistically modeled full system, but without taking delamination into account (Lucchini et al., 2016; Hsu et al., 2009; Hsu et al., 2010; Li and Suo, 2006), others focus purely on the delamination itself using cohesive zone models, where a comparison is made with peel test results (Hoefnagels et al., 2010; van der Sluis et al., 2018), however, no realistic stretchable interconnect geometries under real loading conditions are considered. Therefore, there is a gap in the literature with respect to comparison of experimental data to numerical modeling of full stretchable electronics systems, while taking all the main deformation modes, including delamination and buckling, into account. This gap is particularly pronounced for micron-scale stretchable interconnects. In general, comparison of three-dimensional full-field displacement data with numerical simulations is only done for single materials (Bergers et al., 2014; Bertin et al., 2016) and not for multi-material samples to the best of our knowledge. This work aims at the experimental-numerical characterization of interface delamination in stretchable electronics, where the numerical model is a true representation of the real experiment at the micron-scale. To this end, in situ stretching experiments are performed on aluminum-polyimide stretchable electronic interconnects underneath a confocal optical microscope to measure surface topographies at different time increments, see Section 2. A recently developed adaptive isogeometric digital height correlation algorithm (DHC) (Kleinendorst et al., 2016) is used to analyze the three-dimensional surface displacement fields from these height profiles. In Section 3 the deformation behavior is compared to a numerical simulation, which includes the correct sample geometry and boundary conditions from the experiments and cohesive zones for the interface behavior. The model is improved in several steps until the simulation results reflect the experimentally observed deformation modes. Finally, conclusions are drawn in Section 4.

2. Experimental characterization: DHC on profilometry data

In this section the tools required for the experimental characterization of the stretchable interconnects are introduced and the results are presented.

2.1. Samples

The samples consist of a polyimide (PI) substrate, 10 μm thick, with an aluminum (Al) serpentine-shaped, 1 μm thin electrical interconnect deposited on top. This PI-Al material configuration can be manufactured through photo-lithography based micro-fabrication, allowing for smaller sizes and thus a higher density of interconnect features compared to, e.g., the copper-PDMS stretchable interconnects studied in Brosteaux et al. (2007). The samples were micro-fabricated in the same way as presented in Lucchini et al. (2016). A scanning electron microscopy (SEM) image of the sample, with a height pattern needed for DHC deposited on top, in a stretched state is shown in Fig. 1a. Delamination of the interconnect from the substrate is clearly observed. The grain structure of the aluminum layer is analyzed using Electron Backscatter Diffraction (EBSD), see Fig. 1b.

Two different S-shaped interconnect geometries are analyzed, namely the w20r20a120 and the w20r40a180 samples. Fig. 1c displays the geometrical parameters of the samples, i.e., the width (w), radius (r), amplitude (a), and rectilinear arm length (A_{in}) of the stretchable interconnect, clarifying the names of the different samples. Herein, *rectilinear arm* refers to the rectangular part of the interconnect and the bend, or corner, of the S-shaped interconnect is referred as the *curvilinear* segment. Both samples have an identical rectilinear arm to bend ratio of $\frac{A_{in}}{w+r} = 1$. Based on previous research (Lucchini et al., 2016), a significant difference regarding initiation of the failure mechanisms is expected for the two sample types as a result of the difference in width compared to the other dimensions.

2.2. Experimental setup: in situ profilometry

Tensile experiments on the stretchable electronics samples were performed in situ, i.e., the samples were stretched using a micro-tensile device placed underneath an optical profilometer, see Fig. 2. The samples were glued (using Loctite® 401) on disposable PMMA grippers as shown in the inset of Fig. 2. The grippers and sample were then installed in a Kammrath&Weiss micro-tensile stage equipped with a 50 N load cell to impose a uniaxial tensile deformation. A displacement rate of 1 μm/s was employed. Surface topographies, to be analyzed later with a digital height correlation (DHC) algorithm in order to obtain the full-field 3D deformation behavior of the stretchable interconnects, were acquired by a confocal optical profilometer (Sensofar Pl μ 2300) in intervals of approximately 2% elongation. Tensile deformation was prolonged until 40% applied global strain. For optimal DHC results, the highest spatial resolution is beneficial, therefore a 150X objective with 0.95 aperture was used to collect the surface height profiles, ensuring the largest magnification and numerical aperture. This resulted in a field of view of 85 μm in x-direction by 64 μm in y-direction (768×576 pixels), which is sufficient to capture the buckling and delamination phenomena of the interconnect in the rectilinear arm area.

For each interconnect geometry three repetitions of the experiment were performed to study the reproducibility of the experimental method and results. As discussed in Bergers et al. (2011), obtaining stable and reproducible measurements using optical profilometry remains a challenge. To increase stability and reproducibility of the topographic images, the following measures were applied. First, vibrations and drift of the positioning stage of the confocal optical profilometer, onto which the micro-tensile stage is placed, were eliminated by fixing tilt of the positioning stage (using support at the four corner points) to the rigid vibration isolated base of the profilometer, while still allowing translational movements of the micro-tensile stage. Second, a custom-developed auto-FOV algorithm was employed to automatically establish the same field of view (FOV) between increments. Third, stress relaxation is expected from PI material; preliminary measures showed that equilibrium is achieved within three minutes. On this basis, in order to have reproducible topographic images, acquisitions

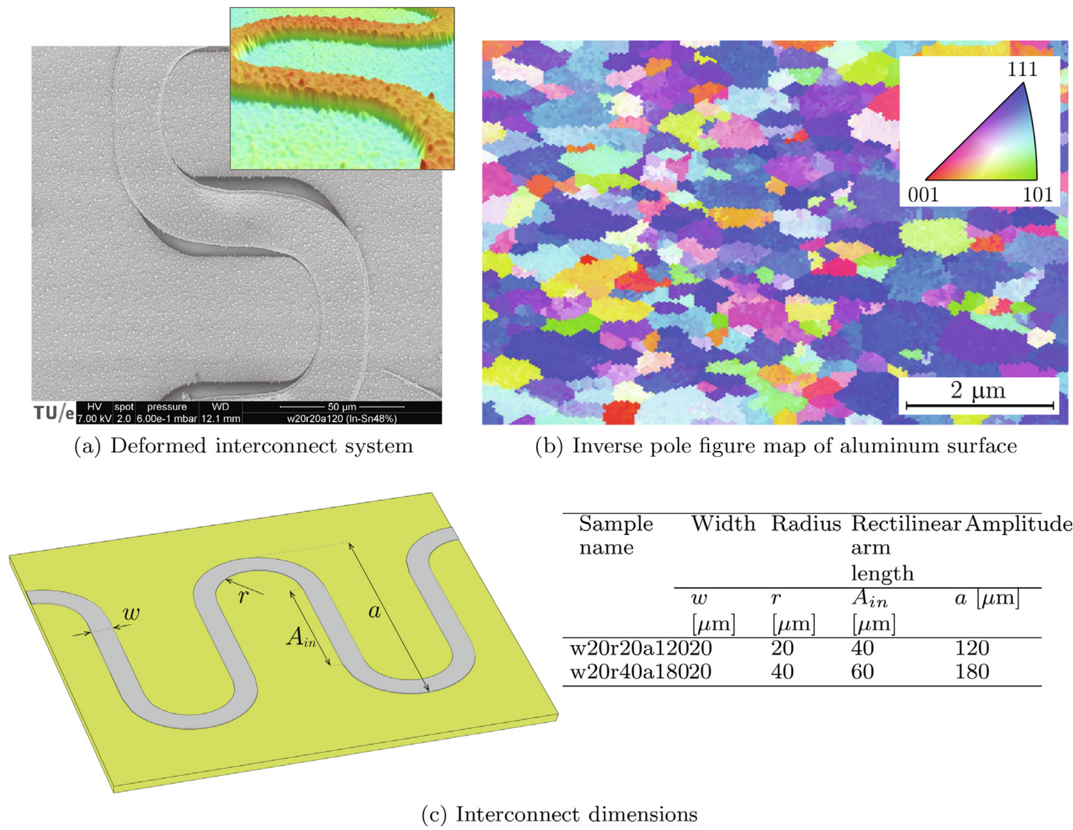

Sample name	Width	Radius	Rectilinear arm length	Amplitude
	w [μm]	r [μm]	A_{in} [μm]	a [μm]
w20r20a120	20	20	40	120
w20r40a180	20	40	60	180

Fig. 1. (a) SEM image of the deformed specimen (with applied height pattern for DHC on top), in which delamination of the interconnect from the substrate is clearly observed. Inset: side view of a surface height profile of the undeformed interconnect system with DHC pattern, showing that the interconnect lies on top of the substrate. (b) OIM micrograph of the top surface of the aluminum interconnects, in which grain coloring is conform the inverse pole figure of the specimen's normal. (c) S-shaped interconnect geometry with indicated geometrical parameters: width (w), internal radius (r), amplitude (a), and rectilinear arm length (A_{in}) for the w20r20a120 and w20r40a180 sample.

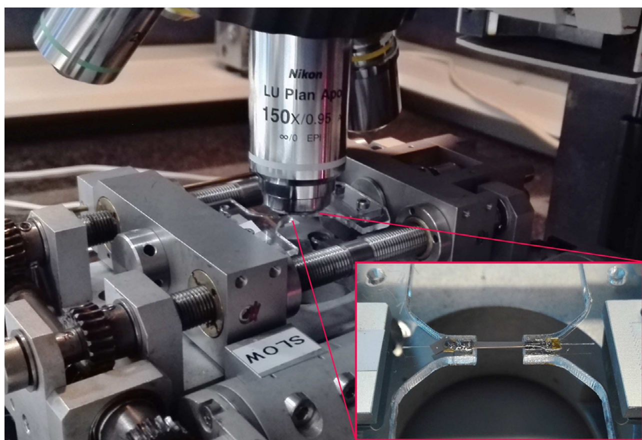

Fig. 2. In-situ configuration of the tensile stage with sample under the 150× objective of the profilometer. The inset shows a sample glued on disposable PMMA grippers.

with confocal laser scanner were taken with a three minute delay. Fourth, the "confocal smoothing" option in the (proprietary) Sensofar software is used as this was found to slightly increase the reproducibility of the measurements as it seems to be sensitive to small-scale noise generated by the steep features of the pattern. Finally, before correlation, topographic images were blurred using a Gauss filter (kernel size 10 pixels and $\sigma = 2$), which was shown to improve robustness of the correlation.

2.3. Digital height correlation

2.3.1. Pattern application

For digital image correlation (or *height* correlation in this case) a distinct speckle pattern is required to distinguish between material points. The stretchable electronics samples considered here have smooth surfaces and hence (almost) no natural texture due to surface roughness that could be used as a speckle pattern. Therefore, an artificial pattern was applied on the PI-Al samples. In the literature, a variety of techniques for applying a three-dimensional speckle pattern can be found, such as the application of several types of particles in a solvent, e.g., ink particles, copper or silver nanoparticles (Hoefnagels et al., 2010). Based on preliminary attempts, neither of these techniques appeared suitable for PI-Al samples, due to agglomeration of the particles at edges of the aluminum interconnect and to the difficulties with obtaining a homogeneous distribution of particles on the interconnect, as well as on the substrate surface. Furthermore, the large difference in reflective properties between the polyimide substrate and the aluminum interconnect are expected to yield complications for the confocal microscopy technique, hence, a pattern that covers the entire surface is desirable. Therefore, we employ a recently developed method, based on DC magnetron sputter deposition of an InSn pattern, which enables the deposition of a scalable height pattern that can easily be tuned to the particular microscopic technique and to the field of view with pixel size that is employed (Hoefnagels et al., 2019). For this particular application, a pattern with a relatively large feature size is needed for optimal correlation of surface height profiles measured with optical profilometry. This pattern

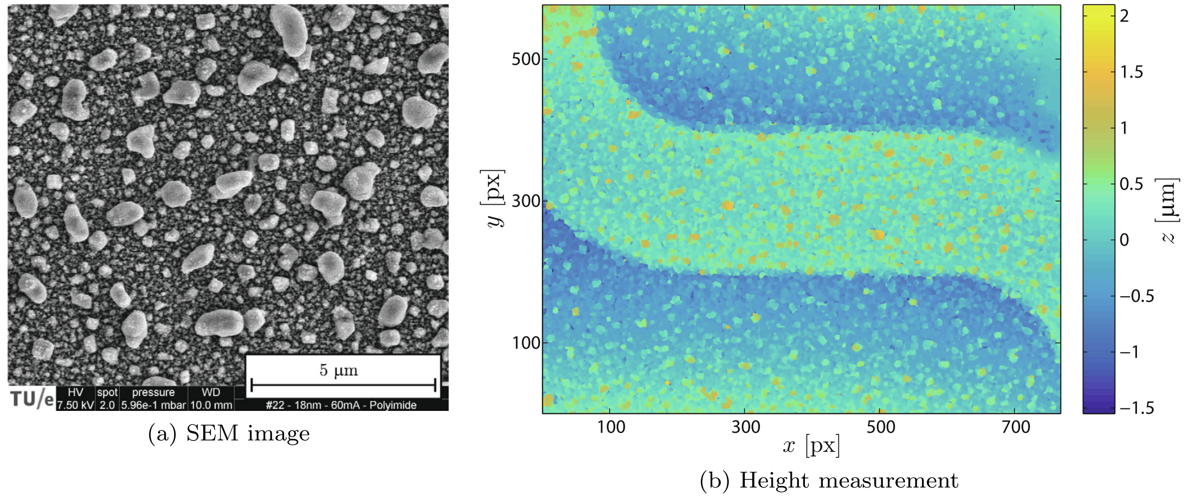

Fig. 3. The resulting height contrast of the Indium-Tin (InSn) sputter deposition layer: (a) Image taken with scanning electron microscopy (SEM), (b) Surface height profile measured with a confocal optical profilometer (150X objective).

is achieved with a low chamber pressure of 8 mTorr and substrate temperature of 80 °C (note that this is well below the processing temperature of the stretchable interconnect samples to prevent alteration of the interface properties), while the deposition rate was regulated by first using a 20 mA target current for 2 min, followed by 60 mA for 7 min. Details on this specific pattern and the employed patterning technique in general are provided in Hoefnagels et al. (2019). The obtained height pattern shows distinct InSn particles of 0.9 μm, see Fig. 3. It was also demonstrated that this pattern does not significantly influence the mechanical behaviour of the stretchable interconnects.

2.3.2. DHC method

To analyze the three-dimensional displacement field of the sample surface during the tensile experiments, digital height correlation is employed. DHC is an extended digital *image* correlation technique, in which height profiles, taken for example using an optical profilometer or an atomic force microscope, are correlated in order to track both the in-plane and out-of-plane displacements of the considered surface (van Beeck et al., 2014; Neggers et al., 2014; Bergers et al., 2014; Kleinendorst et al., 2016). Correlation is based on the minimization of the residual height profile(s) r, which is defined as:

$$r(\underline{x}) = f(\underline{x}) - (g(\underline{x}) \circ \underline{\Phi}(\underline{x}) + U_z(\underline{x})) \approx 0 \quad (1)$$

$$\underline{\Phi}(\underline{x}) = \underline{x} + \underline{U}_{xy}(\underline{x}), \quad (2)$$

with $\underline{x}$ the image coordinates, $f(\underline{x})$ and $g(\underline{x})$ the height profiles in undeformed and deformed configuration respectively, $\underline{U}_{xy}(\underline{x})$ and $U_z(\underline{x})$ the in-plane and out-of-plane displacement components, respectively, and $\underline{\Phi}$ the so-called mapping function that maps the deformed height profile back to the undeformed configuration in order to compare it to the undeformed height profile. The residual approaches zero when the displacements are calculated correctly. However, this is an intrinsically ill-posed problem, since the number of unknowns (i.e., three-dimensional displacements per pixel) exceeds the number of equations (i.e., one scalar residual height value per pixel). Commonly, this is solved by limiting the number of unknowns by means of an approximation of the displacement field with a linear combination of basis functions. It is, however, very important that these basis functions allow for a description which is rich enough to capture the kinematics in the considered problem. In this case the deformation of the stretchable interconnect entails localized buckling, which calls for a specialized discretization of the displacement field. In this work the DHC approach from Kleinendorst et al. (2016) is adopted, which makes use of an adaptive refinement scheme to autonomously refine the basis functions locally, thereby attaining an optimal discretization of the displacement field. This is convenient, since the exact location of the buckles is difficult to predict and may differ from experiment to experiment, whereas manual construction of a suitable set of basis functions is challenging and largely requires user expertise on the problem.

2.4. Results

The tensile experiment was executed and the topography was measured at several load increments. The resulting height profiles for the load increment of 35% applied global elongation on the edges of the sample are shown in Fig. 4. Here the localized buckles, i.e., the typical failure mechanism for these geometries, can clearly be seen. In the same Figure also the displacement fields as calculated with the DHC method, both in-plane (u and v) and out-of-plane (w), are depicted. The 3D displacement field is calculated both for the aluminum interconnect and the adjacent polyimide substrate, to account for all deformation modes occurring in the sample, including delamination between the interconnect and substrate.

From the horizontal displacements, i.e., u, it can be derived that both the substrate and the interconnect contract in this direction, due to the Poisson effect upon elongation in the perpendicular y-direction. This Poisson effect is especially strongly present in the substrate, but because the interconnect is adhered to it, contraction is also conveyed, to lesser extent, to the stiffer interconnect. From the v-displacement mainly rotation of the interconnect towards the direction of elongation can be observed, along with delamination of the interconnect and substrate. The discontinuity in the displacement field between the substrate and the interconnect reveals this delamination. Delamination can also be recognized in the topographic images on top in Fig. 4, as unpatterned substrate area has been revealed at the edges of the aluminum interconnect, while this area was located underneath the interconnect before deformation (hence, no pattern was deposited here). The out-of-plane displacement, i.e., w in the bottom of the Figure, clearly shows the buckles in the Al interconnects: the yellow area denotes upward displacement which is discontinuous with respect to the adjacent PI surface. Multiple measurements and displacement field calculations for different samples of the same geometries revealed a significant variation in the exact locations and height of the buckles, caused by

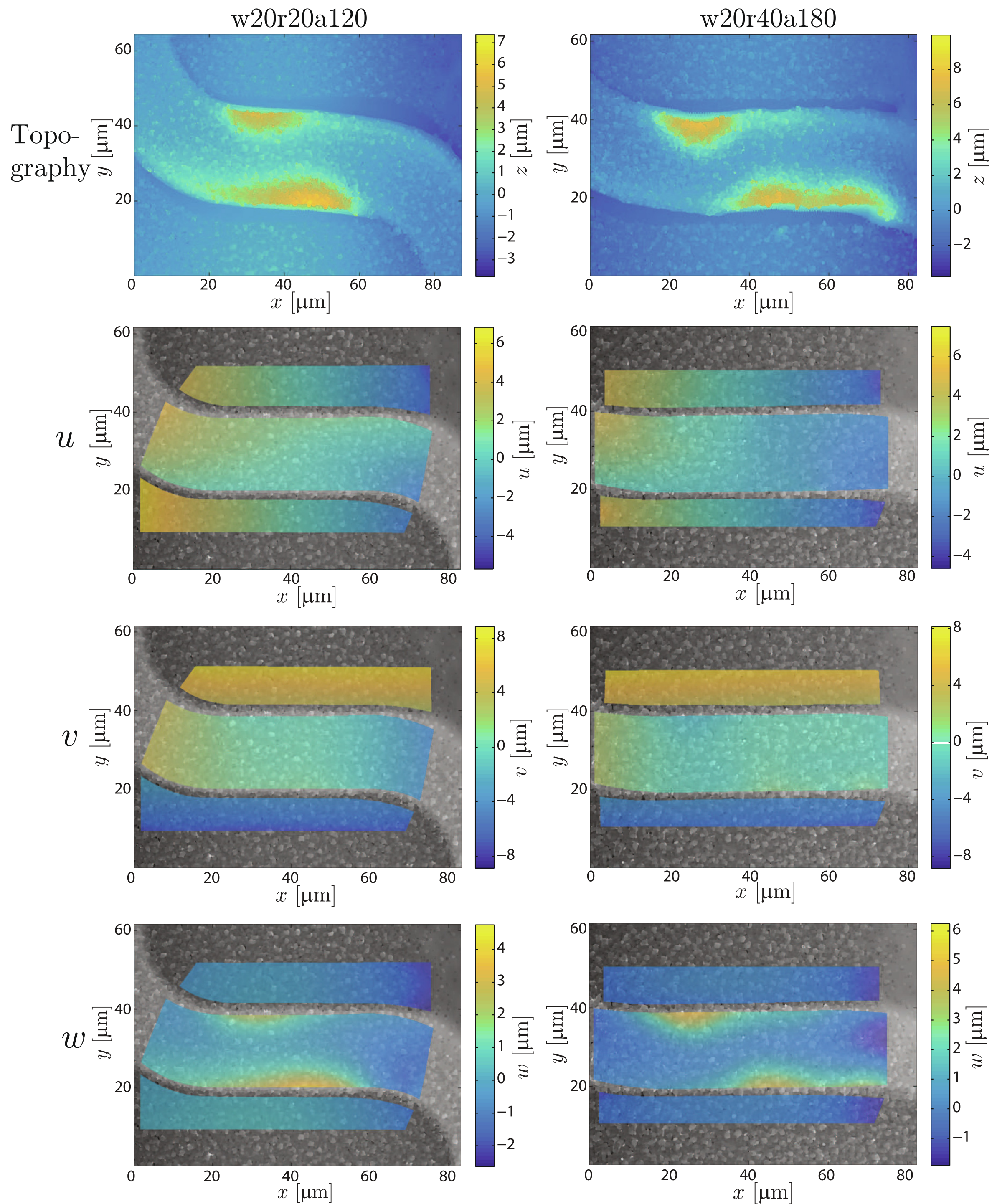

Fig. 4. Acquired surface height profiles (top) for the w20r20a120 and w20r40a180 geometries, at 35% elongation of the total sample, applied in the *y*-direction. Furthermore, plotted on top of a grayscale representation of the undeformed topography, the displacements *u* (in *x*-direction), *v* (*y*-direction) and *w* (out-of-plane, *z*-direction), as calculated with the adaptive DHC method, are shown for both geometries. The displacements are calculated for a region of interest both on the aluminum interconnect and on the polyimide substrate.

stochastic variations in the heterogeneous interface properties (Cattarinuzzi et al., 2015). Because the precise interface heterogeneity is unknown for each sample, it is not very meaningful to perform a one-on-one quantitative, absolute comparison between the measured displacement fields and the ones resulting from a numerical simulation. It is more meaningful to analyse several representative scalar indicators for the mechanical behavior of the samples that are extracted from the full-field displacement information. In Fig. 5 these descriptive parameters are introduced. For the in-plane behavior the contraction δ_U and the rotation ϕ of the rectilinear arm part (line AB in Fig. 5) are monitored during loading. For the out-of-plane behavior the normal opening δ_n of the interface between the aluminum interconnects and the polyimide substrate is measured.

For both geometries the experiment is performed three times and the results in terms of the scalar parameters are shown in

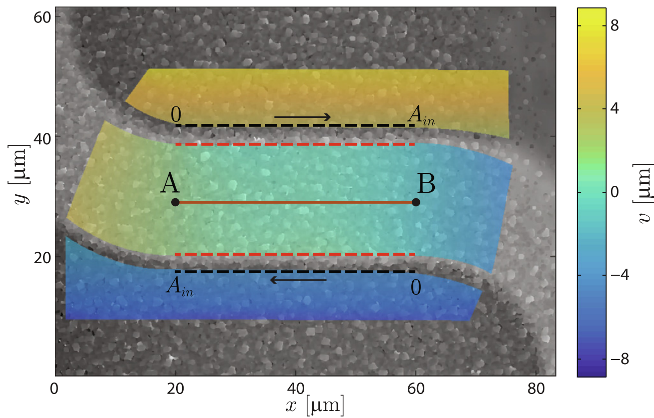

Fig. 5. Explanatory figure for the descriptive parameters of the mechanical behavior of the electronic interconnect during stretch, that are extracted from the full-field displacement information. The in-plane behavior is characterized by the contraction δ_U and rotation ϕ of the rectilinear arm part AB (orange line). The out-of-plane behavior is described by the normal opening δ_n of the interface, i.e., the buckle height along the path $0 - A_{in}$ (where A_{in} is the rectilinear arm length) at the edge of the aluminum interconnect (red dashed lines), corrected with the substrate curvature, i.e., the height profile of the PI substrate along the same path (black dashed lines).

Figs. 6 and 7 for the in-plane (δ_U, ϕ) and out-of-plane (δ_n) behavior respectively. A good repeatability between the individual experiments is observed for the w20r20a120 geometry, while the w20r40a180 sample exhibited a larger scatter in terms of in-plane rotation and normal opening. Especially, the location of the buckles differs significantly from specimen to specimen, as follows from Fig. 7(d) and (f).

Figs. 6 and 7 show that the delamination between the aluminum interconnects and the polymide substrate is the most important mechanism occurring during stretching. Delamination occurs when the interface stresses exceed the interface bonding strength. In these particular samples the polyimide substrate is relatively stiff in comparison to other commonly used substrate materials, e.g., PDMS and TPU. Therefore, the polyimide reacts to the deformation of the stiff metal interconnect with higher stresses compared to other, more compliant substrate materials. This induces high stresses on the interface, making this interface more susceptible to delamination. Comparing Fig. 6(a) and (b), it is observed that contraction in the rectilinear arm is larger in the w20r40a180 sample, which is to be expected since the rectilinear arm part is longer in this geometry (60 µm vs. 40 µm). According to Lucchini et al. (2016) the rectilinear arm length (A_{in}) has a large influence on the delamination mechanism of the aluminum/polyimide interface. For longer A_{in} ($>$ 40 µm) the lateral contraction of the arm outweighs the axial stretching of the underlying polyimide substrate and the delamination is buckling-based, while for shorter interconnects the axial stretch is relatively large with respect to the lateral compression and the delamination is more shear-based, resulting in a more homogeneous delamination front. Because of this more homogeneous delamination, the interconnect

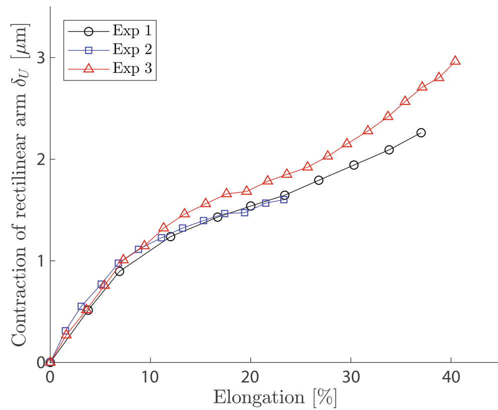

(a) Rectilinear arm contraction δ_U, w20r20a120

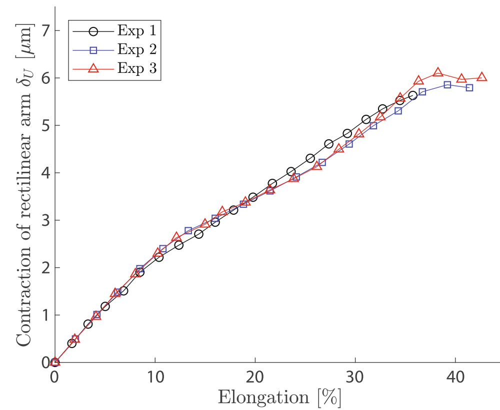

(b) Rectilinear arm contraction δ_U, w20r40a180

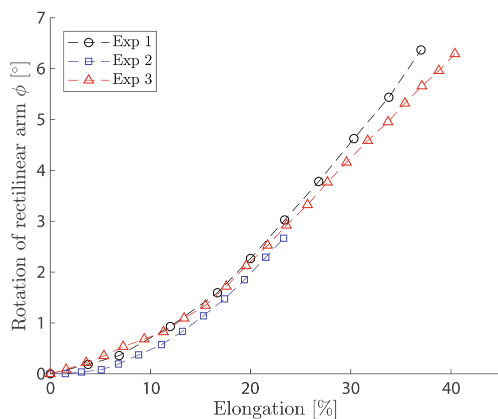

(c) Rectilinear arm rotation ϕ, w20r20a120

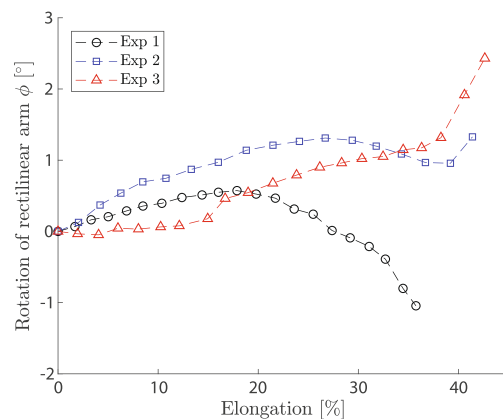

(d) Rectilinear arm rotation ϕ, w20r40a180

Fig. 6. The in-plane behavior as characterized by the descriptive parameters δ_U and ϕ (defined in Fig. 5) for both the w20r20a120 (left) and w20r40a180 (right) geometries. The parameters are plotted for all captured load increments, ranging from 0% to 40% global stretch of the specimen. The data from all three experiments with each sample are shown.

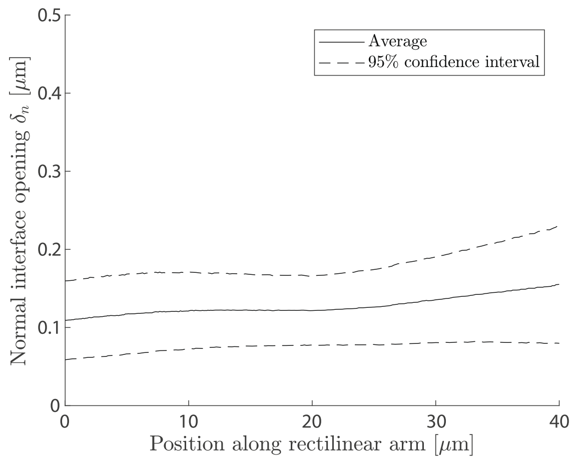

(a) 7% global stretch, w20r20a120

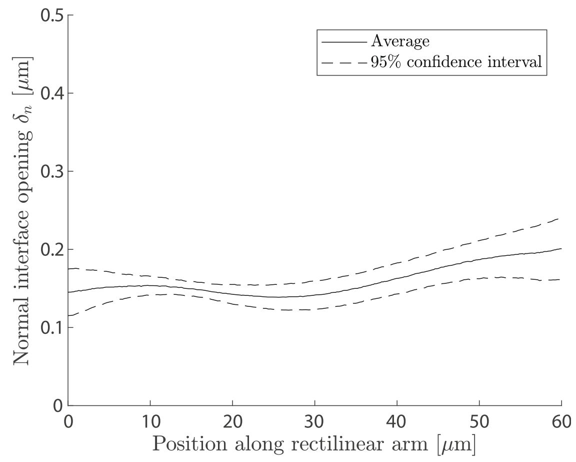

(b) 7% global stretch, w20r40a180

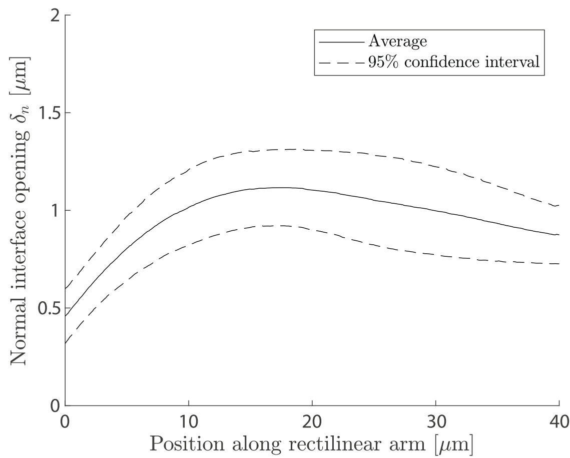

(c) 20% global stretch, w20r20a120

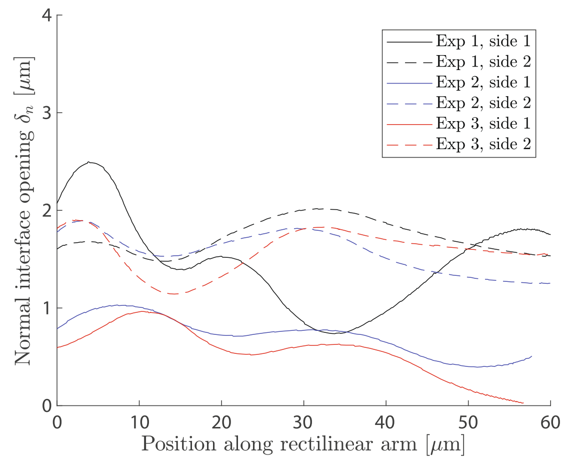

(d) 20% global stretch, w20r40a180

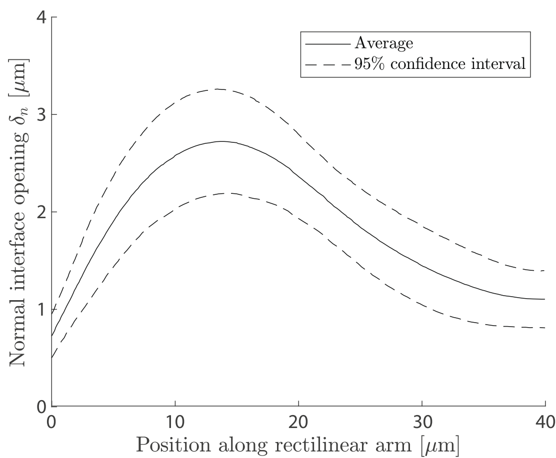

(e) 35% global stretch, w20r20a120

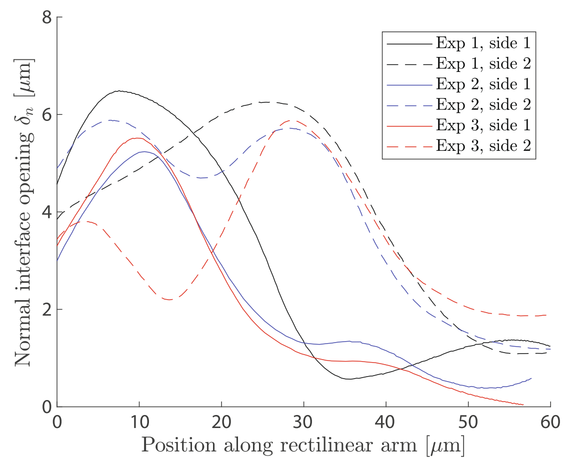

(f) 35% global stretch, w20r40a180

Fig. 7. The out-of-plane behavior as characterized by the normal opening of the interface (defined in Fig. 5) for both the w20r20a120 (left) and w20r40a180 (right) geometries. The normal opening δ_n is plotted as profile along the rectilinear arm length for load increments of 7%, 20% and 35% global stretch respectively. In Figures (a), (b), (c) and (e) the profile is shown as an average of the six measurements (two sides for each of the three specimen) with a 95% confidence interval, to illustrate the good agreement between the experiments. For Figures (d) and (f) the profiles from all measurements are shown separately, because the location of the buckles differs too much to make the average value representative.

has more freedom to rotate with respect to the substrate, which is indeed observed when comparing Fig. 6(c) and (d). Also the observation that the buckle locations are less predictable for the longer rectilinear arm lengths (see Fig. 7(d) and (f)) follows from the fact that the buckling-driven delamination for this geometry is more susceptible to small variations in the heterogeneous interface behavior.

3. Numerical simulations

Numerical simulations are a powerful tool to assess the behavior of the stretchable electronics structures for a wide range of interconnect geometries in addition to time-consuming experiments. From numerical results, delamination and buckling phenomena can be studied to predict failure and eventually optimize the design. However, a suitable model for the mechanical response of the materials is required that has to be validated with respect to experimental data of the interconnects.

The three-dimensional finite element model shown in Fig. 8, developed by Lucchini (2014), is used as a starting point for calibration with the experimental data presented in the previous Section. All finite element models have been developed by using the commercial code ABAQUS[2] model. A submodeling approach is used to increase computational efficiency while maintaining accurate prescription of boundary conditions. In the global part of the model two periods of the interconnect geometry and the underlying substrate, which are assumed to be rigidly bonded, are modeled. Symmetry and periodic boundary conditions are used, see Fig. 8, and the displacements are prescribed using a reference point.

The material properties are not necessarily the same as for the bulk material because of size effects in the miniaturized microsystem. The yield strength of the aluminum interconnect may be affected, since the relative size of the grains with respect to the specimen dimension increases and, therefore, the number of grain boundaries over the cross-section decreases (Janssen et al., 2008). Since the grain boundaries act as pinning points for dislocations, a high density of them delays the onset of plasticity, following the well-known Hall-Petch effect. Consequently, the large amount of free surface (and thus the low number of grain boundaries) in these micron-sized structures results in a lower yield strength of the material, with a possible reduction of the yield strength of aluminum to as low as 5 MPa (Janssen et al., 2008). The material properties of the aluminum interconnect and polyimide substrate were determined previously by means of nano-indentation tests (Lucchini, 2014), and a good agreement was found with an elasto-plastic material model for both materials, with Young's modulus $E = 72$ GPa, Poisson ratio $\nu = 0.34$ and initial yield strength $\sigma_{y0} = 50$ MPa for the aluminum and $E = 3.2$ GPa, $\nu = 0.3$ and $\sigma_{y0} = 20$ MPa for the polyimide. The grain size distribution was measured using EBSD, see Fig. 1b, from which it is concluded that the grain size is in the order of 200–600 nm. This implies that a considerable amount of grain boundaries is available, also over the thickness, (i.e., the grains are not columnar), to impede dislocation movement. Hence, the determined initial yield strength of σ_{y0} = 50 MPa, which is slightly lower than the 70 MPa value for bulk material, is not surprising. Moreover, it has been tested (not shown here) that the exact value of aluminum yield strength has only a minor effect on the delamination behavior, i.e., the interface behavior.

The displacement resulting from the FE simulation with this preliminary global model are prescribed at the lateral boundaries of the local model, which is a representation of only half a period of the interconnect featuring a finer mesh. In the local model the behavior of the interface between the substrate and the interconnect is described by a cohesive zone model with a bilinear traction separation law (TSL), in which all dissipative mechanisms of the interface are lumped. The parameters in this model are the maximum traction τ_{max}, the work of separation G_c (also known as fracture energy, interfacial toughness or critical energy release rate) and the critical opening displacement δ_c. The work of separation was determined by Cattarinuzzi (2016) using 90° peeltests and was estimated at $G_c = 37$ J/m^2. This value is used in all simulations in this paper. It is worth mentioning that, to estimate this value, plastic dissipation of the peel arm (owed to bending at the delamination front (Kim and Aravas, 1988) was accounted for by elastic plastic analysis of the bent shape of the peel arm (Kawashita et al., 2005), which was captured in situ by SEM imaging during the tests. As previously mentioned, the kinematics of PI is not markedly influenced by the presence of the Al interconnect, owed to the stiffness ratio between Al and PI and the thickness of the metal film compared to the substrate. For this reason, the local boundary conditions applied on the PI boundaries are likely to be reliable even when estimated from a global model with the assumption of perfect bonding between Al and PI. The optimal values for the other two parameters are studied by performing simulations on the w20r20a120 geometry while varying τ_{max} and δ_c and comparing the results to the corresponding experimental results from the previous Section, see Fig. 9. It can be seen that the in-plane rotation of the rectilinear arm ϕ can be fitted quite well with a suitable choice of the maximum traction and critical opening displacement ($\tau_{max} = 20$ MPa, $\delta_c = 1$ μm). In contrast, the buckle height is severely underestimated for all investigated combinations. The maximum traction appears to have a larger effect on the behavior, whereas the value for the critical opening displacement is less important. Although the critical opening displacement of 1 μm gives a slightly better fit for the in-plane behavior and the buckle height is not captured well for all combinations, the *location* of the buckle crest seems marginally more accurate for $\delta_c = 0.1$ μm. The same observations are made for the w20r40a180 geometry (the results are not shown here). Therefore, a key ingredient seems to be missing in the model. In the following Sections potential causes for the underestimation of the normal opening displacement are investigated, i.e., residual stresses in the Al/PI system, crystal plasticity of the aluminum interconnects and mixed-mode interface behavior.

3.1. Residual stress

The first effect that is not taken into account in the initial simulations is residual stress. Since the FE model underestimates the opening due to the absence of Al buckling, introducing a compressive residual stress in the Al layer may increase the chance to observe Al buckling in FE analysis, which may testify that residual stresses were the missing ingredient in the numerical analysis. Residual stress in miniaturized systems contributes to the reliability and has been reported as a possible primary source of failure for microelectronic systems (Guo et al., 1993). Residual stress in the Al/PI stretchable electronic system can occur due to the curing process of polyimide and the deposition of the aluminum interconnect layer. During the curing cycle of polyimide intrinsic residual stresses are introduced in the substrate. Residual stresses ranging between 4 and 40 MPa were reported for a 10 μm thick PI layer depending on the temperature cycle of the curing process (Chung et al., 1999). In addition, thin film deposition of the metal layer causes compressive residual stresses in the aluminum film due to mismatch in the coefficient of thermal expansion (CTE) (Soroka et al., 2010). When the Al/PI interconnect system is lifted off the silicon wafer in the final processing stage, the residual stress in the PI substrate and Al film result in a curvature due to the equili-

[2] Dassault Systèmes Simulia©, Providence, RI, US.

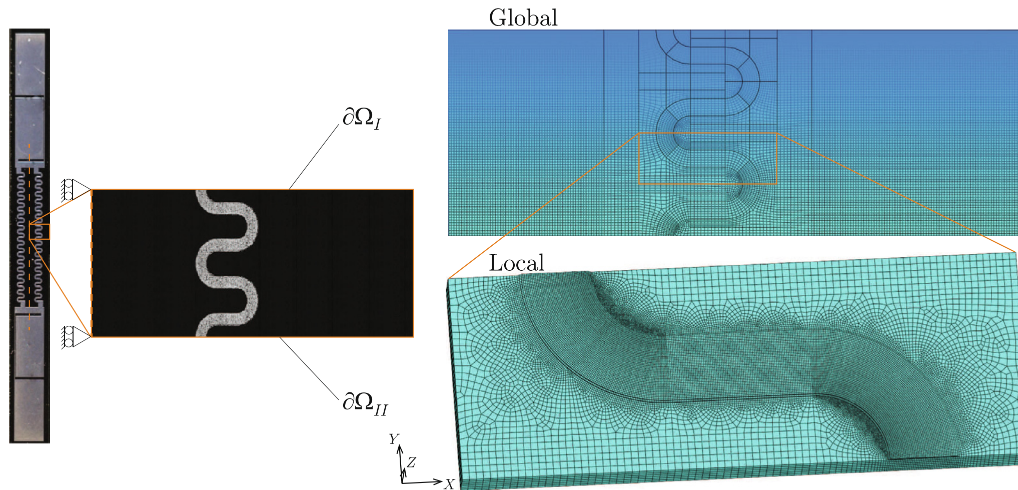

Fig. 8. Submodeling approach of the finite element model. On the left side a microscopic photograph of an entire specimen is displayed, with a zoom-in on two periods of the aluminum interconnect. On the right side the global model of the same two periods is shown, with the interconnect rigidly bonded to the substrate, which is constructed by using symmetry of the sample (orange dotted line) and periodic boundary conditions on the top and bottom edges $\partial\Omega_I$ and $\partial\Omega_{II}$. The resulting displacements (in x, y and z direction) are prescribed at the lateral boundaries of the local model, which entails half a period of the interconnect, with the interconnect bonded to the substrate with a cohesive zone description.

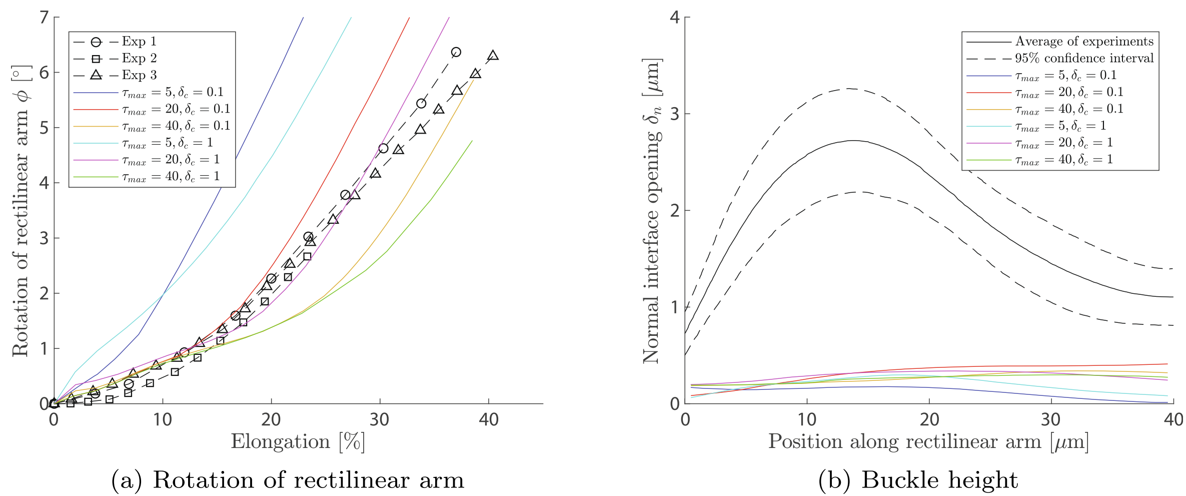

Fig. 9. Comparison of the (a) in-plane rectilinear arm rotation and (b) the out-of-plane buckling height at 35% globally applied elongation between experiments (data from Fig. 5) and numerical simulations using a bilinear TSL. The legend shows the interface properties used for the different simulations, with τ_{max} in MPa and δ_c in μm.

bration of the stress state. The residual stress is added to the local numerical model by lumping the intrinsic and thermal residual stress into a single thermal residual stress introduced in the Al/PI system prior to elongation. This thermal stress is induced in the model by a thermal step while the boundaries of the local model are confined, mimicking that the stretchable interconnect system is still bonded on the silicon wafer. The magnitude of that theoretical thermal step is determined by the measurement of the curvature of a 10 μm thick PI substrate, fully coated with a 1 μm thick deposited Al layer. The reason for performing this curvature measurement on the fully coated sample is as follows. When fabricated together, fully coated and patterned Al/PI samples will exhibit a difference residual curvature for the same driver of misfit, i.e. the thermal load. Yet, the analytical curvature analysis (Evans and Hutchinson, 1995) only holds for flat films on substrates. Therefore, instead of measuring the residual curvature directly from the Al/PI pattern, the residual curvature is measured for a fully coated Al/PI sample and used to estimate an equivalent thermal load as a driver of misfit. Subsequently the same thermal load has been introduced in the Al/PI local model to test its influence on the kinematics of the interconnect. To estimate the eligible thermal load for simulating residual stresses in the patterned interconnect, the topography of a fully coated Al/PI sample has been measured right after lift off from the carrier Si wafer, yielding a curvature of $\kappa = -5.2 \cdot 10^{-4}$ μm^{-1}. The thermal load required to achieve the measured curvature has been estimated following (Evans and Hutchinson, 1995), obtaining $\Delta T = -450$ K. The consistency of the analytical estimate has been verified by means of a 2D plane strain FE analysis of a Al/PI bilayer upon thermal load, yielding the same curvature within the uncertainty bound. The same thermal load was used to induce a residual stress field in the local model of the Al/PI interconnect right before stretching. More precisely, the numerical simulation of the stretchable interconnect is executed as described earlier, with the traction separation law parameters that gave the best fit for the in-plane behavior, i.e., $G_c = 37$ J/m^2, $\tau_{max} = 20$ MPa, $\delta_c = 1$ μm, and with the thermal step of -450 K prior to elongation. Fig. 10 shows a comparison of FE analysis results with and without residual stresses, using the inter-

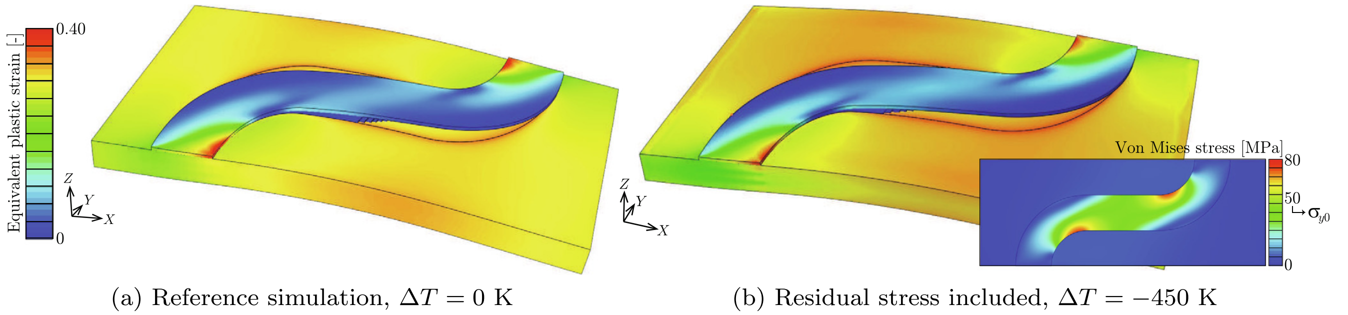

Fig. 10. FEM results (equivalent plastic strain) for the local model of the w20r20a120 geometry with the reference model (a) and the model where a thermal pre-step of −450 K is included to account residual stress (b). In the inset in (b) the Von Mises stresses resulting from the thermal pre-step are shown.

face parameters best matching the in-plane experimental descriptors. The stress is concentrated at the transitions between the rectilinear arm and inner radius of the curvilinear segments (see inset in Fig. 10 and exceeds the yield strength of the aluminum interconnect, resulting in local plastic deformation in this area. However, upon stretching of the interconnect system the induced plasticity seems to have a negligible effect on the delamination and buckling behavior, and as a result the normal opening remains severely underestimated. Therefore, it is concluded that thermal stress (although its magnitude could not be explicitly estimated for the specific structure) may not play a relevant role in determining the mode I opening of the buckled film owed to the resilience of the aluminum, i.e. its capability to accommodate the misfit through plastic strain.

3.2. Mixed mode interface behavior

Finally, the effect of a mixed-mode cohesive zone model on the interconnect deformations is studied. When studying the tractions on the interface just before the onset of delamination in more detail, it becomes apparent that the normal tractions are a factor 4 lower than the tractions in shear mode. This results in pure shear delamination, which induces rotation of the rectilinear arm, accompanied by slight out-of-plane twisting of the curvilinear part, however, no extensive out-of-plane deformation of the rectilinear arm. Therefore, to capture the experimentally observed large buckling behavior of the interconnects, it appears to be necessary to promote mode I delamination over mode II delamination, by imposing different properties of the traction separation law in shear mode and normal mode, see Fig. 11.

In this mixed-mode interface model the traction separation laws are defined by means of the work of separation G_c, maximum traction τ_{max} and critical opening displacement δ_c, which are defined separately for both modes. Shear behavior is modeled isotropically, the damage criterion is based on maximum stress and damage evolution is based on the energy that is dissipated during the damage process (the fracture energy). The effective critical energy scales linearly between the pure normal and pure shear thresholds, as a function of mode mixity. The latter is measured as the relative contribution of the current pure shear mode (G^s) to the current total energy ($G^T = G^s + G^n$). More details can be found in Dassault Systèmes Simulia (2020). In this work, δ_c is assumed to be mode-angle independent and taken 0.05 µm, because some preparatory research with the mixed-mode framework revealed that $\delta_c = 0.05$ µm gives slightly better results in terms of the out-of-plane deformation than $\delta_c = 1$ µm and $\delta_c = 0.1$ µm, which were studied earlier, although it was found again that the value of δ_c only has a minor influence on the delamination and buckling behavior. As mentioned above, the work of separation in mode I, G_c^n, was determined by 90° peeltests by Cattarinuzzi (2016) and

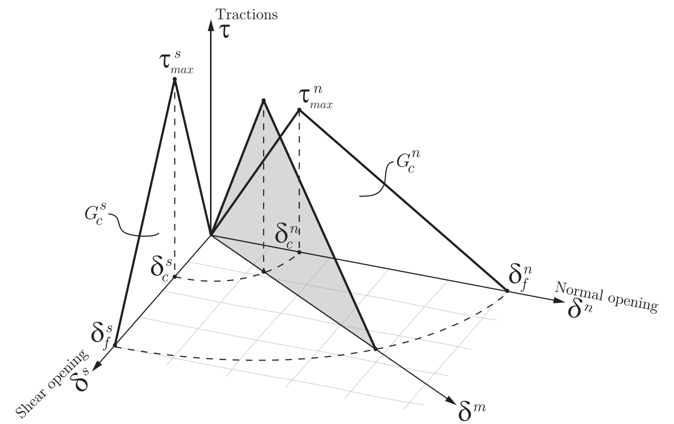

Fig. 11. Illustration of a mixed-mode traction separation law as defined in the cohesive zone elements. The parameters are: maximum traction τ_{max}, the work of separation G_c and the critical opening displacement δ_c, where the superscripts n, s and m denote the normal (mode I), shear (mode II) and mixed direction respectively. Also indicated is the final opening, δ_f, which directly results, for each mode angle, from the choice of τ_{max} and G_c. In this work, δ_c is chosen to be mode angle independent, as motivated in the text. This figure is reproduced and slightly adapted from Dassault Systèmes Simulia (2020).

established 37 J/m^2, equal to the value used in the previous simulations. For the remaining parameters, G_c^s, τ^n_{max} and τ^s_{max}, no data is available and their effect is studied. First, the mode I maximum traction of the cohesive zones is lowered with respect to the mode II maximum traction and different ratios and values for τ^n_{max} and τ^s_{max} are tested, see Figs. 12a and 12b. The buckling amplitude is strongly affected positively by a higher ratio of $\tau^s_{max}/\tau^n_{max}$ and the location of the crest shifts more towards the transition from the rectilinear arm to the inner radius of the curvilinear segment, leading to a better agreement with the experimental data. The reason for the shift in crest location is that, with increasing maximum shear traction, delamination is delayed, causing the curvilinear parts of the interconnects to straighten to accommodate stretching of the sample (whereas rotation of the rectilinear arm towards the stretching direction is hindered by interface which is not sufficiently debonded), resulting in compressive stresses in the rectilinear part near the transition region to the inner radius, triggering delamination at this location. For decreasing normal maximum traction, the possibility to delaminate in mode I increases in this region, resulting in the observed behavior of Fig. 12b.

Not only the ratio, but also the absolute value of the maximum traction is important. For lower absolute values of τ^s_{max} mode II delamination at the outer radius of the curvilinear segments is still energetically more favorable and a lower buckling amplitude is observed, see the difference between $\tau^s_{max}/\tau^n_{max} = 20/4$ and $\tau^s_{max}/\tau^n_{max} = 30/6$, which have the same ratio, but different absolute

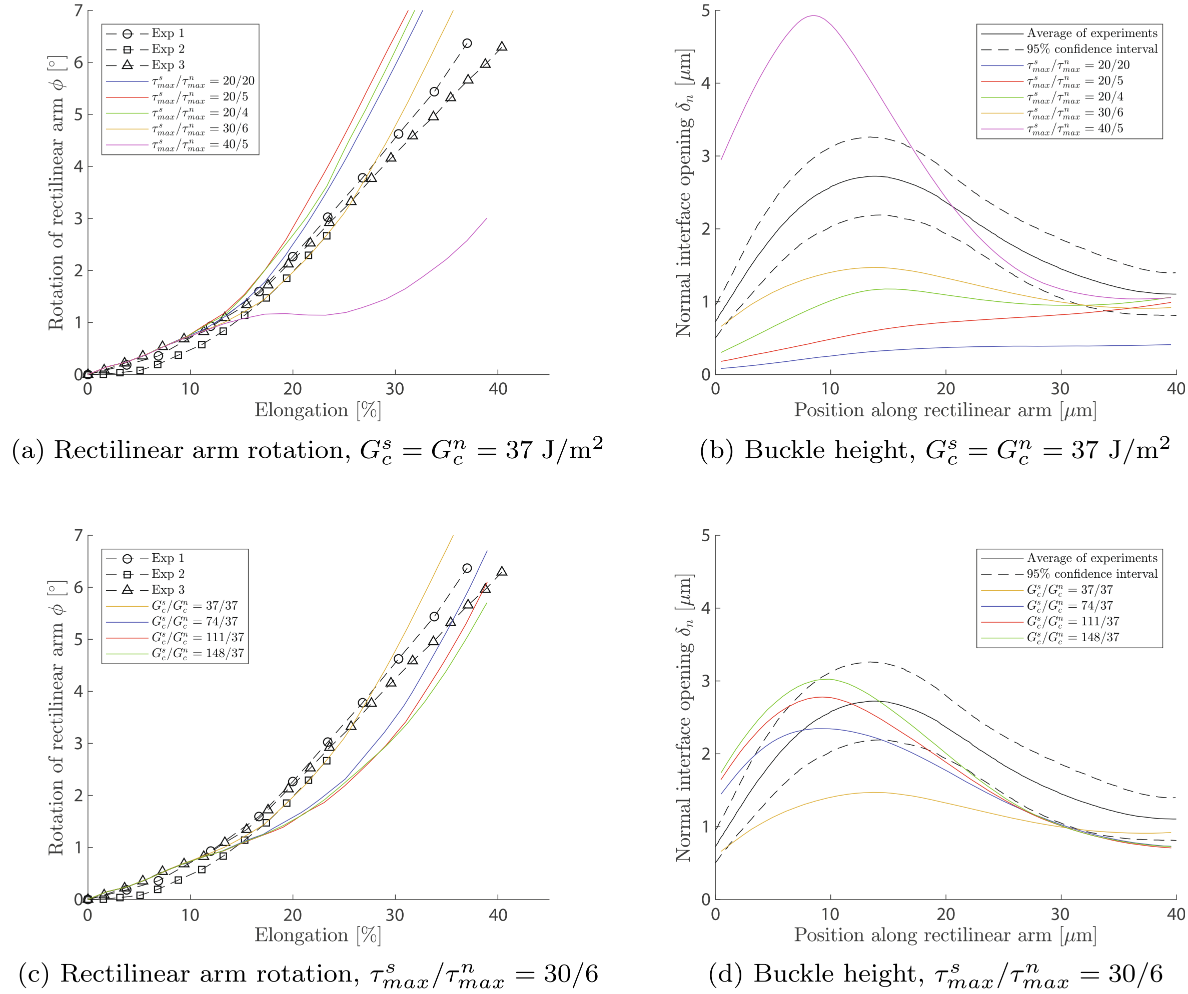

(a) Rectilinear arm rotation, $G^s_c = G^n_c = 37$ J/m^2 (b) Buckle height, $G^s_c = G^n_c = 37$ J/m^2

(c) Rectilinear arm rotation, $\tau^s_{max}/\tau^n_{max} = 30/6$ (d) Buckle height, $\tau^s_{max}/\tau^n_{max} = 30/6$

Fig. 12. Comparison of the (a and c) in-plane rectilinear arm rotation and (b and d) the out-of-plane buckling height at 35% globally applied elongation between experiments (data from Fig. 5) and numerical simulations with different ratios of the traction separation law properties. In the first set of simulations (a and b) the work of separations is kept equal for both modes and the maximum traction are varied. In the second set (c and d) the best fit for the tractions ($\tau^s_{max}/\tau^n_{max} = 30/6$) is used, while the mode II work of separation G^s_c is varied.

values. More and earlier mode I delamination in the rectilinear arm also reflected in the decrease of rotation of this part, see Fig. 12a, which is especially noticeable for an extremely high shear maximum traction versus low normal maximum traction ($\tau^s_{max}/\tau^n_{max} = 40/5$).

Next, the work of separation in shear mode, G^s_c, is studied. The best fit from the previous experiment, i.e., $\tau^s_{max} = 30$ MPa, $\tau^n_{max} = 6$ MPa, is selected for these new simulations. The resulting rectilinear arm rotation and buckle profiles are shown in Figs. 12a and 12d. An increase in G^s_c (for a fixed τ^s_{max}) means a retardation of final failure in shear mode. Consequently, failure in normal mode is promoted, which results again in higher buckling amplitudes and less rotation of the rectilinear arm. For the tested values of $G^s_c, G^s_c = 111$ J/m^2 seems to yield the best quantitative agreement between the simulation and the experiments in terms of both the in-plane and out-of-plane displacements. A value of G^s_c that is three times higher than G^n_c seems well possible, as such a ratio has been observed frequently in the literature, e.g., (Hutchinson and Suo, 1991; Ruybalid et al., 2019).

In summary, a good match with the experiments is found for simulation with a mixed-mode cohesive zone model, with the parameters as listed in Table 1. The resulting geometry from the FEM simulation is shown in Fig. 13a, where is it compared to the experimentally measured height profile. Also, a predictive simulation is performed with the same interface parameters, but for the w20r40a180 geometry, see Fig. 13b. In both cases a good qualitative agreement between the simulation and experiment is achieved, i.e., the buckle amplitude, location and number of crests are highly comparable.

Table 1
List of the mixed-mode traction separation law parameters used in the cohesive zone model that best fits the experimental data.

Parameter		Normal direction (mode I)	Shear direction (mode II)
Work of separation	G_c	37 J/m^2	111 J/m^2
Maximum traction	τ_{max}	6 MPa	30 MPa
Critical opening displacement	δ_c	0.05 µm	0.05 µm

It should be noted that the selected values for the interface properties provide a good, but not perfect fit. Qualitatively, the main cause for the observed deformation behavior was found to be a difference in interface properties between normal and shear direction, i.e., the presence of mixed-mode behavior. Quantitatively, however, the simulations do not exactly equate the observed deformation. Yet, it does not appear to be useful to improve the model further, since the variability in experimental results is relatively high. A perfect fit for one particular experiment would yield a poor prediction

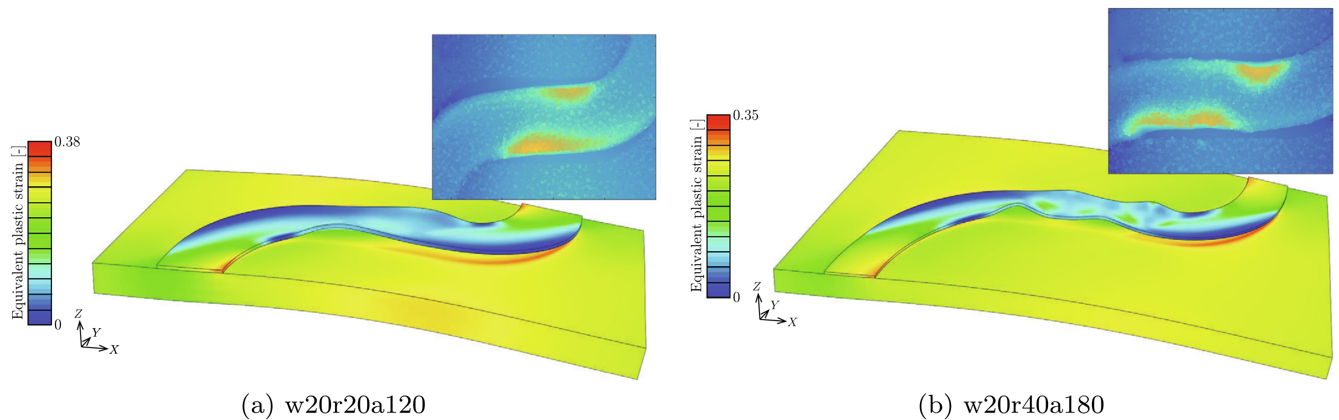

Fig. 13. FEM results (deformed geometry and equivalent plastic strain) with the mixed-mode cohesive zone model for both geometries. For comparison, the insets show the topographic height profile measurements from the experiments at the same global stretch increment.

for another experiment with the same parameters. Moreover, the goal of this work was not to find a perfect numerical model, but to reveal the underlying cause for the observed buckling behavior in order to gain insight in the failure mechanism of these stretchable interconnects.

The mode sensitivity found in this study may be explained by the absence of fibrillation during interface delamination. In Neggers et al. (2015) it was found that mode sensitivity is negligible in the considered PDMS-copper interface, because of the complex geometry of the rough copper surface and consequently the alignment of the fibrils with the traction direction. In case of the here examined polyimide-aluminum system, the aluminum has a relatively smooth surface, as observed by a homogeneous peelfront in mode I peeltests (Cattarinuzzi et al., 2015). This may explain the observed much higher mode angle dependency, caused by significant energy dissipation by friction under shear loading, resulting in the experimentally measured deformation profiles.

4. Conclusions

Delamination and buckling phenomena, which are known to affect the reliability of stretchable electrical interconnect structures, have been studied by the use of in-plane and out-of-plane descriptors of the deformed geometry of two interconnect geometries upon tensile stretching. This data was obtained by the acquisition of surface height profiles upon stretch using confocal optical profilometry for an in situ experimental setup. These height profiles were then correlated using adaptive isogeometric digital height correlation to obtain three-dimensional displacement fields of the surface of the aluminum-polyimide interconnect structure. From the derived three-dimensional displacement fields it was shown that delamination initiates at approximately 7% global elongation for both sample types. A sufficiently large delaminated area under the rectilinear arm is accompanied by a significant rotation of the rectilinear arm which was observed at 18% global elongation for the w20r20a120 geometry and at global strain levels beyond 35% for the w20r40a180 interconnect geometry. In addition, approximately semicircular buckles nucleate along the rectilinear arm at roughly 15%–18% global elongation as a result of lateral compression of the delaminated Al film at the rectilinear arm. This can be attributed to the Poisson compression of the substrate and by a localized region of compression at the transition between rectilinear arm and inner bend of the curvilinear segment. Moreover, the buckling amplitude and pattern were shown to differ between the sample types, which is assigned to the difference of the rectilinear arm length A_{in}.

A numerical model was developed to capture the in-plane and out-of-plane behavior of the stretchable interconnect upon elongation. It was demonstrated that a simple bilinear traction-separation law without mode dependency is insufficient to capture the characteristic buckling behavior of the Al-PI interconnects. Moreover, implementation of residual stress and the effect of a free surface size effect, by lowering the yield strength of aluminum were all shown to be insufficient to capture the experimentally observed behavior of the stretchable interconnects. However, a fair qualitative agreement of the in-plane and out-of-plane behavior of the interconnect has been reached by adopting a mixed-mode cohesive zone model. Characteristic buckling behavior is captured by the numerical model only when the ratio between shear and normal maximum traction is substantially increased. A $\tau^s_{max}/\tau^n_{max}$ ratio of 30 MPa to 6 MPa and work of separation of $G^n_c = 37$ J/m^2 and $G^s_c = 111$ J/m^2 seems to yield the best fit of in-plane and out-of-plane deformations of the interconnect of the w20r20a120 geometry to the experiments. Also a predictive simulation with the same parameters for the w20r40a180 geometry yields a good qualitative agreement with the experimental data.

The mode angle dependency may be caused by the low surface roughness of the metal film and the consequential absence of fibrillation. The results of this study could, e.g., be used to improve the processing of the interconnect system, such that the interface toughness in normal direction increases and the mode sensitivity is lowered, which could be realized by manufacturing a fibrillating interface. This would lead to a promotion of shear delamination, causing more rotation of the rectilinear arms with respect to the substrate. Consequently, the high stress concentrations and plastic strains found at the inner bend of the curvilinear parts could be lowered, which improves the durability of the interconnects. That makes this an interesting region for further analysis for a possible optimization of the interconnect design for delayed failure and higher stretchability.

Declaration of Competing Interest

The authors declare that they have no known competing financial interests or personal relationships that could have appeared to influence the work reported in this paper.

Acknowledgement

The research of S.M. Kleinendorst and J.P.M. Hoefnagels was funded by the Netherlands Organization for Scientific Research (NWO) under the VIDI scheme (project number STW12966).

Cristian Collini, Andrea Adami and Leandro Lorenzelli (Microsystems Technology Research Unit, Fondazione Bruno Kessler, Trento, IT) are greatly acknowledged for their contribution concerning the micro-fabrication of stretchable interconnect samples.

References

Bergers, L.I.J.C., Hoefnagels, J.P.M., Delhey, N.K.R., Geers, M.G.D., 2011. Measuring time-dependent deformations in metallic MEMS. Microelectron. Reliab. 51 (6), 1054–1059. https://doi.org/10.1016/j.microrel.2011.03.008.

Bergers, L.I.J.C., Hoefnagels, J.P.M., Geers, M.G.D., 2014. Characterization of time-dependent anelastic microbeam bending mechanics. J. Phys. D: Appl. Phys. 47, 1–14. https://doi.org/10.1088/0022-3727/47/35/355306.

Bertin, M., Du, C., Hoefnagels, J.P.M., Hild, F., 2016. Crystal plasticity parameter identification with 3D measurements and Integrated Digital Image Correlation. Acta Mater. 116, 321–331. https://doi.org/10.1016/j.actamat.2016.06.039.

Brosteaux, D., Axisa, F., Gonzalez, M., Vanfleteren, J., 2007. Design and fabrication of elastic interconnections for stretchable electronic circuits. IEEE Electron. Device Lett. 28 (7), 552–554. https://doi.org/10.1109/LED.2007.897887.

Cattarinuzzi, E., 2016. In-situ Mechanical Characterization of Deformable Metal/Polymer Electrical Interconnects (Ph.D. thesis). Politecnico di Milano..

Cattarinuzzi, E., Lucchini, R., Gastaldi, D., Vena, P., Lorenzelli, L., Hoefnagels, J.P.M., 2015. In-situ experimental characterization of interfacial toughness of aluminum thin films on polyimide substrates. In: 20th International Conference on Composite Materials: 19-24th July 2015, Copenhagen..

Cattarinuzzi, E., Lucchini, R., Gastaldi, D., Vena, P., 2015 Design of aluminum/polyimide stretchable interconnects investigated through in-situ testing. In: XVIII AISEM Annual Conference.https://doi.org/10.1109/AISEM.2015.7066784. .

Chung, H., Joe, Y., Han, H., 1999. The effect of curing history on the residual stress behavior of PI thin films. J. Appl. Polym. Sci. 74 (14), 3287–3298.

Dassault Systèmes Simulia. Abaqus 6.13 software. User manual;http://dsk.ippt.pan.pl/docs/abaqus/v6.13/books/usb/default.htm. (Interactions; Contact Property Models; Mechanical Contact Properties; Surface Based Cohesive Behavior; Damage Evolution; Mixed Mode Definition). .

Evans, A.G., Hutchinson, J.W., 1995. The thermomechanical integrity of thin films and multilayers. Acta Metall. Mater. 43 (7), 2507–2530. https://doi.org/10.1016/0956-7151(94)00444-M.

Gonzalez, M., Axisa, F., Vanden Bulcke, M., Brosteaux, D., Vandevelde, B., Vanfleteren, J., 2008. Design of metal interconnects for stretchable electronic circuits. Microelectron. Reliab. 48, 825–832. https://doi.org/10.1016/j.microel.2008.03.025.

Gray, D.S., Tien, J., Chen, C.S., 2004. High-conductivity elastomeric electronics. Adv. Mater. 16 (5), 393–397. https://doi.org/10.1002/adma.200306107.

Guo, Q., Keer, L.M., Chung, Y.W., 1993. Thermal Stress and Strain in Microelectronics Packaging. Publisher: Van Nostrand Reinhold, New-York. Ch. 10: Thermal Stress-Induced Open-Circuit Failure in Microelectronics Thin-Film Metallizations. pp 329–359. .

Gutbrod, S.R., Sulkin, M.S., Rogers, J.A., Efimov, I.R., 2014. Patient-specific flexible and stretchable devices for cardiac diagnostics and therapy. Prog. Biophys. Mol. Biol. 115, 244–251. https://doi.org/10.1016/j.pbiomolbio.2014.07.011.

Harris, K.D., Elias, A.L., Chung, H.-J., 2016. Flexible electronics under strain: a review of mechanical characterization and durability enhancement strategies. J. Mater. Sci. 51 (6), 2771–2805. https://doi.org/10.1007/s10853-015-9643-3.

Hoefnagels, J.P.M., Neggers, J., Timmermans, P.H.M., van der Sluis, O., Geers, M.G.D., 2010. Copper-Rubber interface delamination in stretchable electronics. Scr. Mater. 63 (8), 875–878. https://doi.org/10.1016/j.scriptamat.2010.06.041.

Hoefnagels, J.P.M., van Maris, M.P.F.H.L., Vermeij, T., 2019. One-step deposition of nano-to-micron-scalable, high-quality digital image correlation patterns for high-strain in-situ multi-microscopy testing. Strain e12330. https://doi.org/10.1111/str.12330.

Hsu, Y.-Y., Gonzelez, M., Bossuyt, F., Axisa, F., Vanfleteren, J., de Wolf, I., 2009. In situ observations on deformation behavior and stretching-induced failure of fine pitch stretchable interconnect. J. Mater. Res. 24 (12), 3573–3582. https://doi.org/10.1557/jmr.2009.0447.

Hsu, Y.-Y., Gonzalez, M., Bossuyt, F., Axisa, F., Vanfleteren, J., de Wolf, I., 2010. The effect of pitch on deformation behavior and the stretching-induced failure of a polymer-encapsulated stretchable circuit. J. Micromech. Microeng. 20, (7) 075036.

Hutchinson, J.W., Suo, Z., 1991. Mixed mode cracking in layered materials. Adv. Appl. Mech. 29, 63–191. https://doi.org/10.1016/S0065-2156(08)70164-9.

Janssen, P.J.M., Hoefnagels, J.P.M., de Keijser, T.H., Geers, M.G.D., 2008. Processing induced size effects in plastic yielding upon miniaturisation. J. Mech. Phys. Solids 56 (8), 2687–2706. https://doi.org/10.1016/j.jmps.2008.03.008.

Kawashita, L.F., Moore, D.R., Williams, J.G., 2005. Analysis of peel arm curvature for the determination of fracture toughness in metal-polymer laminates. J. Mater. Sci. 40, 4541–4548. https://doi.org/10.1007/s10853-005-0856-8.

Kim, K.-S., Aravas, N., 1988. An elastoplastic analysis of the peel test. Int. J. Solids Struct. 24 (4), 417–435. https://doi.org/10.1016/0020-7683(88)90071-6.

Kim, D.-H., Lu, N., Ma, R., Kim, Y.-S., Kim, R.-H., Wang, S., Wu, J., Won, S.M., Tao, H., Islam, A., Yu, K.J., Kim, T.-I., Chowdhury, R., Ying, M., Xu, L., Li, M., Chung, H.-J., Keum, H., McCormick, M., Liu, P., Zhang, Y.-W., Omenetto, F.G., Huang, Y., Coleman, T., Rogers, J.A., 2011. Epidermal electronics. Science 333, 838–843. https://doi.org/10.1126/science.1206157.

Kim, D.H., Lu, N., Ghaffari, R., Kim, Y.S., Lee, S.P., Xu, L., Wu, J., Kim, R.H., Song, J., Liu, Z., Viventi, J., Graff, B., Elolampi, B., Mansour, M., Slepian, M.J., Hwang, S., Moss, J.D., Won, S.M., Huang, Y., Litt, B., Rogers, J.A., 2011. Materials for multifunctional balloon catheters with capabilities in cardiac electrophysiological mapping and ablation therapy. Nat. Mater. 10(4), 316-232.https://doi.org/10.1038/nmat2971..

Kleinendorst, S.M., Hoefnagels, J.P.M., Fleerakkers, R.C., van Maris, M.P.F.H.L., Cattarinuzzi, E., Verhoosel, C.V., Geers, M.G.D., 2016. Adaptive isogeometric digital height correlation: application to stretchable electronics. Strain 52 (4), 336–354. https://doi.org/10.1111/str.12189.

Klinker, L., Lee, S., Work, J., Wright, J., Ma, Y., Ptaszek, L., Webb, R.C., Liu, C., Sheth, N., Mansour, M., Rogers, J.A., Huang, Y., Chen, H., Ghaffari, R., 2015. Balloon catheters with integrated stretchable electronics for electrical stimulation, ablation and blood flow monitoring. Extreme Mech. Lett. 3, 45–54. https://doi.org/10.1016/j.eml.2015.02.005.

Koh, A., Kang, D., Xue, Y., Lee, S., Pielak, R.M., Kim, J., Hwang, T., Min, S., Banks, A., Bastien, P., Manco, M.C., Wang, L., Ammann, K.R., Jang, K.-I., Won, P., Han, S., Ghaffari, R., Paik, U., Slepian, M.J., Balooch, G., Huang, Y., Rogers, J.A., 2016. A soft, wearable microfluidic device for the capture, storage, and colorimetric sensing of sweat. Sci. Transl. Med. 8, 366ra165.

Li, T., Suo, Z., 2006. Deformability of thin metal films on elastomer substrates. Int. J. Solids Struct. 43 (7–8), 2351–2363. https://doi.org/10.1016/j.ijsolstr.2005.04.034.

Li, T., Suo, Z., Lacour, S.P., Wagner, S., 2005. Compliant thin film patterns of stiff materials as platforms for stretchable electronics. J. Mater. Res. 20 (12), 3274–3277. https://doi.org/10.1557/jmr.2005.0422.

Lipomi, D.J., Chong, H., Vosgueritchian, M., Mei, J., Bao, Z., 2012. Toward mechanically robust and intrinsically stretchable organic solar cells: Evolution of photovoltaic properties with tensile strain. Solar Energy Mater. Solar Cells 107, 355–365. https://doi.org/10.1016/j.solmat.2012.07.013.

Lucchini, R., 2014. Mechanics of Stretchable Interconnects for Stretchable Electronics Devices (Ph.D. thesis). Politecnico di Milano..

Lucchini, R., Cattarinuzzi, E., Maraghechi, S., Gastaldi, D., Adami, A., Lorenzelli, L., Vena, P., 2016. Delamination phenomena in aluminum/polyimide deformable interconnects: In-situ micro-tensile testing. Mater. Design 89, 121–128. https://doi.org/10.1016/j.matdes.2015.09.086.

Neggers, J., Hoefnagels, J.P.M., Hild, F., Roux, S., Geers, M.G.D., 2014. Direct stress-strain measurements from bulged membranes using topography image correlation. Exp. Mech. 54 (5), 717–727. https://doi.org/10.1007/s11340-013-9832-4.

Neggers, J., Hoefnagels, J.P.M., van der Sluis, O., Geers, M.G.D., 2015. Multi-scale experimental analysis of rate dependent metal-elastomer interface mechanics. J. Mech. Phys. Solids 80, 26. https://doi.org/10.1016/j.jmps.2015.04.005.

Neggers, J., Hoefnagels, J.P.M., van der Sluis, O., Sedaghat, O., Geers, M.G.D., 2015. Analysis of dissipative mechanisms in metal-elastomer interfaces. Scr. Mater. 149, 412–424. https://doi.org/10.1016/j.engfracmech.2015.06.056.

Quintereo, A.V., Verplancke, R., De Smet, H., Vanfleteren, J., 2017. Stretchable electronic platform for soft and smart contact lens applications. Adv. Mater. Technol. 2 (8), 1–10. https://doi.org/10.1002/admt.201700073.

Rogers, J.A., Bao, Z., 2002. Printed plastic electronics and paperlike displays. J. Polym. Sci. Part A 40 (20), 3327–3334. https://doi.org/10.1002/pola.10405.

Ruybalid, A.P., Hoefnagels, J.P.M., van der Sluis, O., van Maris, M.P.F.H.L., Geers, M.G. D., 2019. Mixed-mode cohesive zone parameters from integrated digital image correlation on micrographs only. Int. J. Solids Struct. 156–157, 179–193. https://doi.org/10.1016/j.ijsolstr.2018.08.010.

Soroka, O.B., Klymenko, S.A., Kopeikina, M.Y., 2010. Evaluation of residual stresses in PVD-coatings. Part 2. Strength Mater. 42 (4), 450–458. https://doi.org/10.1007/s11223-010-9236-y.

Sterken, T., Vanfleteren, J., Torfs, T., Op de Beek, M., Bossuyt, F., Van Hoof, C., 2011. Ultra-Thin Chip Package (UTCP) and stretchable circuit technologies for wearable ECG system. IEEE 33th Engineering in Medicine and Biology Society Conference.https://doi.org/10.1109/IEMBS.2011.6091734. .

Stoppa, M., Chiolerio, A., 2014. Wearable electronics and smart textiles: a critical review. Sensors 14 (7), 11957–11992. https://doi.org/10.3390/s140711957.

van Beeck, J., Neggers, J., Schreurs, P.G.J., Hoefnagels, J.P.M., Geers, M.G.D., 2014. Quantification of three-dimensional surface deformation using global digital image correlation. Exp. Mech. 54 (4), 557–570. https://doi.org/10.1007/s11340-013-9799-1.

van der Sluis, O., Hsu, Y.-Y., Timmermans, P.H.M., Gonzalez, M., Hoefnagels, J.P.M., 2011. Stretching induced interconnect delamination in stretchable electronic circuits. J. Phys. D: Appl. Phys. 44, (3) . https://doi.org/10.1088/0022-3727/44/3/034008 034008.

van der Sluis, O., Vermeij, T., Neggers, J., Vossen, B., van Maris, M.P.F.H.L., Vanfleteren, J., Geers, M.G.D., Hoefnagels, J.P.M., 2018. From fibrils to toughness: multi-scale mechanics of fibrillating interfaces in stretchable electronics. Materials 11 (2), 231. https://doi.org/10.3390/ma11020231.

Vanfleteren, J., Gonzalez, M., Bossuyt, F., Hsu, Y.-Y., Vervust, T., De Wolf, I., Jablonski, M., 2012. Printed circuit board technology inspired stretchable circuits. Mater. Res. Soc. Bull. 37 (3), 254–260. https://doi.org/10.1557/mrs.2012.48.

Yang, Y., Xu, K., Vervust, T., Vanfleteren, J., 2018. Multifunctional and miniaturized flexible sensor patch: design and application for in situ monitoring of epoxy polymerization. Sens. Actuators B: Chem. 261, 144–152. https://doi.org/10.1016/j.snb.2018.01.141.